

Environment-Dependent Stability and Mechanical Properties of DNA Origami Six-Helix Bundles with Different Crossover Spacings

Yang Xin, Petteri Piskunen, Antonio Suma, Changyong Li, Heini Ijäs, Sofia Ojasalo, Iris Seitz, Mauri A. Kostianen, Guido Grundmeier, Veikko Linko,* and Adrian Keller*

The internal design of DNA nanostructures defines how they behave in different environmental conditions, such as endonuclease-rich or low-Mg²⁺ solutions. Notably, the inter-helical crossovers that form the core of such DNA objects have a major impact on their mechanical properties and stability. Importantly, crossover design can be used to optimize DNA nanostructures for target applications, especially when developing them for biomedical environments. To elucidate this, two otherwise identical DNA origami designs are presented that have a different number of staple crossovers between neighboring helices, spaced at 42- and 21- basepair (bp) intervals, respectively. The behavior of these structures is then compared in various buffer conditions, as well as when they are exposed to enzymatic digestion by DNase I. The results show that an increased number of crossovers significantly improves the nuclease resistance of the DNA origami by making it less accessible to digestion enzymes but simultaneously lowers its stability under Mg²⁺-free conditions by reducing the malleability of the structures. Therefore, these results represent an important step toward rational, application-specific DNA nanostructure design.

1. Introduction

DNA-based nanotechnology^[1,2] and the DNA origami technique,^[3–7] in particular, are rapidly approaching real-life biomedical applications.^[8] However, many such applications still face challenges arising from the low stability of DNA nanostructures in biological fluids.^[9,10] The low-Mg²⁺ ion content and the presence of digestion enzymes can lead to the unraveling and structural breakdown of the DNA nanostructures, thus imposing a limit to their lifetime.^[11] Therefore, measures have been taken to protect DNA nanostructures from their environment by encapsulation,^[11–16] by transferring their structural information into other materials,^[17–21] by chemical^[22,23] or enzymatic ligation^[24,25] of the staple strands, or by covalently cross-linking neighboring DNA domains.^[26–29] However, environmental stability is not unambiguous


for all DNA nanostructures. Notably, the shapes and internal structural features have a major effect on how they tolerate, for instance, enzymatic digestion or different buffer conditions.^[30–39] Therefore, DNA origami design choices such as lattice type, staple lengths, crossover location and spacing, twist correction, and so on all affect the structural and mechanical properties and thus the environment-dependent behavior of the nanostructures.^[25,37,39–46] This means DNA stability can be manipulated also by rational design, instead of solely by outer factors. For example, deliberate design can be used for additional benefit in devising tools like drug carriers with engineered release profiles.^[34]

Especially, the inter-helical crossovers that hold the DNA nanostructures together are integral in this capacity. It was recently shown by Chandrasekaran et al.^[38] that an increased number of crossovers directly correlates with significantly increased nuclease resistance in linear, paranemic crossover (PX) DNA nanostructures. For more sophisticated structures such as DNA origami, it is known that the amount of staple crossovers affects their mechanical properties, with less densely populated DNA origami displaying more flexibility and local fluctuation.^[44,47] This flexibility has been shown to play a pivotal role in how accessible the DNA origami are to endonucleases

Y. Xin, C. Li, G. Grundmeier, A. Keller
Technical and Macromolecular Chemistry
Paderborn University
Warburger Str. 100, 33098 Paderborn, Germany
E-mail: adrian.keller@uni-paderborn.de

P. Piskunen, H. Ijäs, S. Ojasalo, I. Seitz, M. A. Kostianen, V. Linko
Biohybrid Materials
Department of Bioproducts and Biosystems
Aalto University
P.O. Box 16100, Aalto 00076, Finland
E-mail: veikko.linko@aalto.fi

A. Suma
Dipartimento di Fisica
Università di Bari and Sezione INFN di Bari
Bari 70126, Italy

 The ORCID identification number(s) for the author(s) of this article can be found under <https://doi.org/10.1002/sml.202107393>.

© 2022 The Authors. Small published by Wiley-VCH GmbH. This is an open access article under the terms of the Creative Commons Attribution-NonCommercial License, which permits use, distribution and reproduction in any medium, provided the original work is properly cited and is not used for commercial purposes.

DOI: 10.1002/sml.202107393

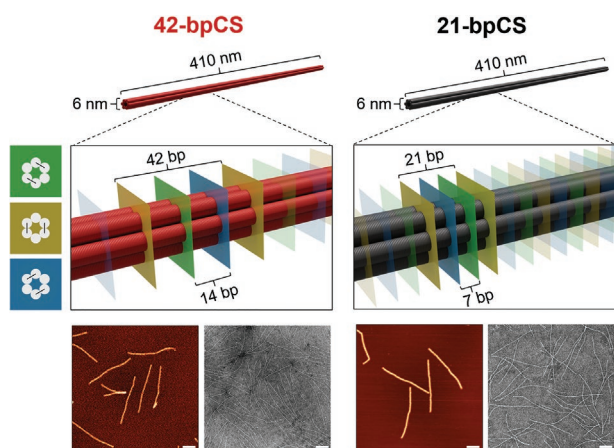


Figure 1. The two six-helix bundle (6HB) designs used in this work. Top panel (left): 6HB with 42-base pair crossover spacings (42-bpCS) (42 bp between crossovers that link the same neighboring helices, which equals 14 bp between any inter-helical crossovers). Top panel (right): 6HB with 21-base pair crossover spacings (21-bpCS) (21 bp between crossovers that link the same neighboring helices, which equals 7 bp between any inter-helical crossover). The inter-helical crossover positions are indicated with the color-coded planes. Bottom panel: Atomic force microscopy (AFM) images of the folded 6HB designs on a mica substrate and transmission electron microscopy (TEM) images ($1 \times 1 \mu\text{m}^2$). The scale bars are 100 nm.

and how the digestion of the structures progresses.^[33] Furthermore, the routing and length of the employed staple strands that constitute the crossovers also contribute to how the structures fold and stay intact at elevated temperatures or in the presence of disruptive environmental factors.^[24,43,48] Even so, while the effects of crossovers on the mechanical properties and environmental stability of DNA nanostructures have been investigated previously, there are no conclusive studies dealing with more complex DNA origami that systematically account for both.

Thus, in this work, we designed two otherwise identical six-helix bundle (6HB) DNA origami nanostructures in a honeycomb lattice that exhibit crossover spacings (CS) (spacings between crossovers that link the same neighboring helices) of either 42 or 21 base pairs (bp) in order to investigate the effects that different CS have on their stability and mechanical properties (Figure 1). Both 6HB designs were subjected to various buffer conditions and enzymatic digestion to compare their biologically relevant environmental stabilities. In addition, molecular dynamics simulations were employed to model the physical characteristics of these two designs. Due to their different CS, the 6HBs behave differently in low- Mg^{2+} environments and they are digested at different rates by DNase I. However, and importantly, denser crossovers do not universally result in better stability. There is, instead, a trade-off between flexibility and accessibility. We found that the 6HB with shorter crossover spacings is less accessible and thus more resistant to DNase I digestion, but it has poor stability under low- Mg^{2+} conditions. Meanwhile, the design with longer crossover spacings has increased flexibility and thus endures increases in electrostatic inter-helical repulsion notably better.

2. Results

2.1. 6HB Designs

The two 6HB DNA origami were created based on the original and widely used 6HB design of Bui et al.^[49] Both the 42-bpCS and 21-bpCS structures consist of a total of 170 staples: 152×42 -nt long core staples, 9×49 -nt long extended staples, and 9×35 -nt long shortened staples. Both designs have identical scaffold routing and permutation. 21-bpCS includes the same crossovers that repeat every 42 bp in 42-bpCS, yet it also features an additional staple crossover between those, resulting in twice the number of crossovers and a spacing of 7 bp instead of 14 bp between any inter-helical crossovers (see Figure 1). Thus, the designs have identical outer dimensions, but presumably different mechanical properties, such as flexibility. The full designs (Figures S1–S4, Supporting Information) along with lists of all used staples sequences, folding optimization (Figure S5, Supporting Information), and additional TEM images (Figures S6 and S7, Supporting Information) are shown in the Supporting Information.

The 18 staples that are not 42 nt long are designed to conform to the original structure by Bui et al. Thus, both structures feature three identical binding sites for modifications such as Au nanoparticles. These sites were formed by shifting the nicks between three pairs of staple strands (between their 3' and 5' ends) at three locations along one helix by 7 nt (one staple shortening and the other elongating by 7 nt, respectively), which results in three binding sites with three available modification handles each (illustrated in Figures S2 and S4, Supporting Information). The longer 49-nt staples could then be extended out of the 6HBs at the 5' end with a desired capture sequence if needed (a 20-nt sticky-end extension was used in the original work by Bui et al.). However, for this study, no such extensions were used for either design. To further comply with the 6HB layout by Bui et al., the helix ends of both designs also contain scaffold loops formed by 109 unpaired scaffold bases (3×24 , 2×8 , and 1×9 nt loops). Finally, the 21-bpCS design has two core staples in a different motif to avoid an otherwise overlapping staple and scaffold crossover (illustrated in Figure S4, Supporting Information).

2.2. Molecular Dynamics Simulations of the 6HBs

We proceed by first characterizing the mechanical stability of 21-bpCS and 42-bpCS 6HBs through molecular dynamics simulations (see Experimental Section). Figure 2a,b shows the snapshots of equilibrated conformations for the two cases, along with zoom-ins with the staple crossovers highlighted in red to visualize the different crossover densities. Figure 2c depicts the distributions of the end-to-end distance (R_{ee}), defined as the distance between two nucleotides on the opposite sides of the bundle along the longitudinal direction (seen in Figure 2a). The 42-bpCS design has both a lower average value and a larger spread, highlighting that the conformation bends more easily than the 21-bpCS one.

In Figure 2d, we present the average, over different sampled configurations, of the tangent–tangent correlation, $\langle \cos\theta(l) \rangle$,

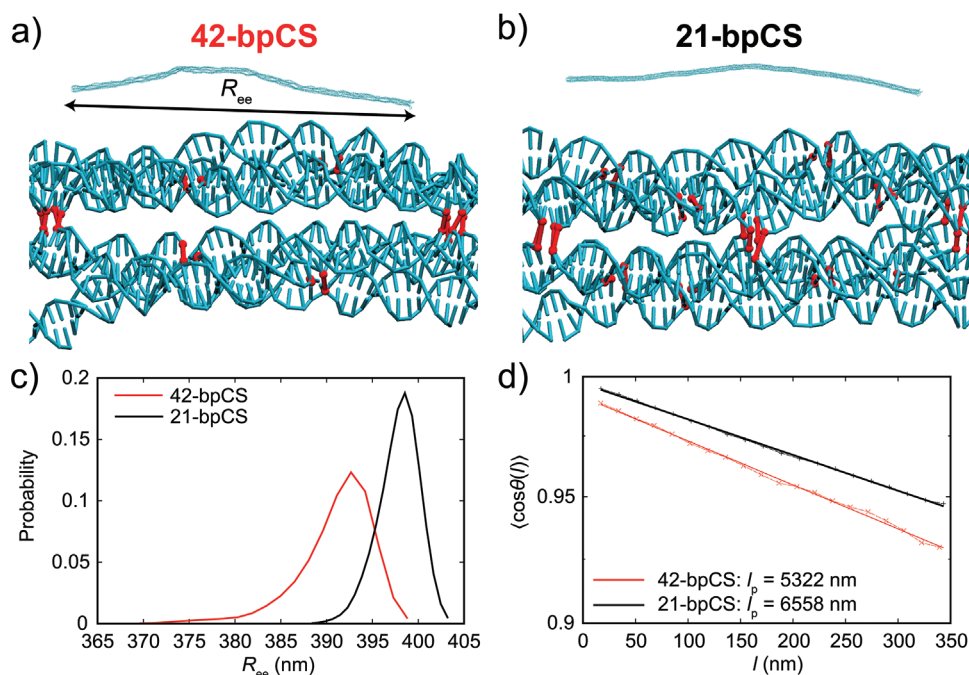


Figure 2. Molecular dynamics simulations of the two different 6HB designs. a, b) Snapshots of equilibrated conformations with zoomed-in sections. The crossovers between the same neighboring helices are highlighted in red. c) Distributions of end-to-end distances (R_{ee}), defined as the distance between two nucleotides on the opposite sides of the bundle along the longitudinal direction. d) The tangent–tangent correlation, $\langle \cos\theta(l) \rangle$, as a function of the chain contour length, l . The fits give the persistence lengths l_p according to Equation (1).

where θ is the angle between tangent directions of any two segments along a 6HB contour separated by an arc length l . The measurement here is made using one of the six DNA centerlines, obtained from a portion of the scaffold which crosses to the other centerlines only at the border of the bundle. A fit of the persistence length l_p has been made using the relation^[50]

$$\langle \cos\theta(l) \rangle = e^{-\frac{l}{s l_p}} \quad (1)$$

where s is a surface parameter; $s = 2$ for the chains equilibrated on a surface (value used for experimental measurements) and $s = 1$ for the chains equilibrated in 3D (which is the case for simulations for a chain fluctuating in three dimensions). We measured the correlation using segment lengths of 50 bp in order to compute the tangent vectors. A segment length exceeding the crossover spacing was chosen to avoid local correlation effects due to local positioning of individual helices between crossovers, although smaller segments still yield similar persistence lengths. According to the fits, the persistence length is slightly higher for 21-bpCS than for 42-bpCS (6558 nm for 21-bpCS vs 5322 nm for 42-bpCS). It was shown by Schiffels et al. that the persistence length of DNA helix bundles depends strongly on the inter-helical spacing, with larger spacings resulting in larger persistence lengths.^[51] For our two designs, this should lead to the 42-bpCS design having a larger persistence length than 21-bpCS, which is obviously not the case. On the contrary, the MD simulations reveal that the persistence length of 42-bpCS is about 20% smaller than that of 21-bpCS. This is probably caused by the additional inter-helical bonds reducing the freedom of movement/fluctuation.

2.3. Stability in Low-Mg²⁺ Environments

To test the stability of the two different 6HB designs in various low-Mg²⁺ environments, we employed an established buffer exchange protocol based on spin filtering.^[32] After assembly in Mg²⁺-containing Tris-acetate-EDTA (TAE) buffer, the 6HBs were thus transferred into low-Mg²⁺ solutions comprising TAE, Tris, H₂O, and different phosphate-based buffers. The residual Mg²⁺ concentration after buffer exchange was $\approx 10 \mu\text{M}$.^[32] The effect of different low-Mg²⁺ environments on the structural integrity of 6HBs was then assessed by atomic force microscopy (AFM) (see Figures S8–S20, Supporting Information). To this end, the samples were mixed with the same Mg²⁺-containing TAE/MgCl₂ buffer employed during DNA origami assembly and immediately afterward adsorbed on mica surfaces. The addition of Mg²⁺ ions was necessary to ensure the efficient immobilization of the negatively charged DNA structures on the like-charged mica surface.^[32,52]

As can be seen in the resulting AFM images shown in **Figure 3**, the two designs behave rather differently in the different solutions. In low-Mg²⁺ TAE buffer, the presence of EDTA (1 mM) leads to the removal of residual Mg²⁺ ions from the DNA's backbone phosphates, which is a determining factor for the structural integrity of the 6HBs. In addition, the presence of acetate ions (20 mM), which shows a remarkable propensity for ion pair formation with Mg²⁺,^[53,54] may also contribute to the depletion of stabilizing Mg²⁺ ions at the DNA backbone. However, whereas the 42-bpCS design remains largely intact and exhibits only some partially molten regions along its axis, the 21-bpCS design is completely denatured so that only the

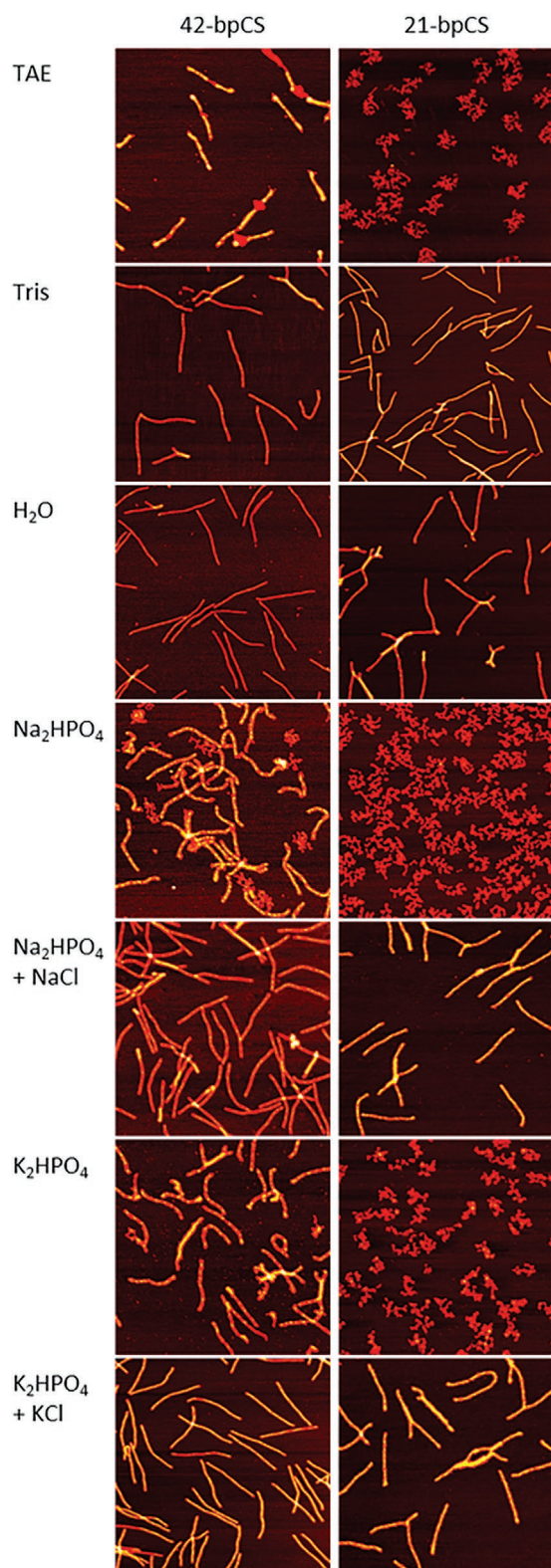


Figure 3. AFM images ($1.5 \times 1.5 \mu\text{m}^2$, height scales 4 nm) of DNA origami 6HBs with different crossover spacings. 6HBs were first transferred into different Mg^{2+} -free solutions as indicated and subsequently adsorbed at mica surfaces by mixing with TAE/ MgCl_2 buffer.

mostly unhybridized scaffolds are visible in the corresponding AFM image in Figure 3.

In a 10 mM Tris buffer without EDTA and also in pure H_2O , both 6HBs appear perfectly stable. In 10 mM Na_2HPO_4 and 10 mM K_2HPO_4 (see Experimental Section and a previous publication for the detailed information of the employed buffers^[32]), the scenario is similar to the case of TAE, that is, the 21-bpCS design is completely denatured, while the 42-bpCS design exhibits a much higher stability. Even though some completely denatured 6HBs can be observed in the AFM images, the majority appear largely intact. The only visible effect of the phosphate buffers on the intact structures is their grainy appearance, which may indicate the onset of denaturation. Denaturation of DNA origami nanostructures in pure phosphate buffers is most likely the result of partially dissociated HPO_4^{2-} ions in solution complexing the phosphate-bound Mg^{2+} ions at the DNA backbone, which reduces their ability to screen electrostatic repulsion between neighboring double helices.^[32] This effect can be compensated by addition of high concentrations of Na^+ or K^+ ions. As can be seen in the corresponding AFM images in Figure 3, structural integrity of both designs is indeed retained in the presence of 200 mM NaCl or KCl.

The results presented in Figure 3 reveal that the crossover spacing has a strong effect on the structural stability in low- Mg^{2+} environments. In particular, it is observed that in critical Mg^{2+} -free buffers, the 42-bpCS design is more stable than 21-bpCS, despite having fewer crossovers. This indicates that the driving force behind DNA origami denaturation under such conditions is indeed electrostatic repulsion between neighboring double helices. DNA origami designs with a lower crossover density are mechanically less rigid and individual double helices have more flexibility. This enables them to respond to a moderate increase in electrostatic repulsion by structural and conformational adjustments instead of duplex unstacking and disintegration. Therefore, the strength of electrostatic inter-strand repulsion between neighboring helices should also affect the overall mechanical properties of the 6HBs. To test this hypothesis, we next attempted to quantify the effect of the different low- Mg^{2+} environments, that do not result in notable DNA origami denaturation, on 6HB flexibility.

When analyzing the mechanical properties of the 6HBs under low- Mg^{2+} conditions, it is crucial that the overall Mg^{2+} concentration is not altered in any way, as this may lead to changes in the strength of electrostatic inter-strand repulsion and thus to alterations of the overall stiffness. This, therefore, prohibits the addition of Mg^{2+} ions to facilitate 6HB adsorption at the mica surface. Instead, we have modified the mica surface with a thin film of the polyamine spermidine, which enables DNA origami adsorption at mica even under essentially Mg^{2+} -free conditions,^[52] as can be seen in the AFM images in Figures S16–S20, Supporting Information. For all conditions chosen, the 6HBs are structurally intact and adsorbed at the spermidine-modified mica surface in more or less comparable density, even though sample-to-sample and image-to-image variations in surface coverage can be rather pronounced. Using such AFM images, we measured the persistence lengths l_p of the 6HBs based on the tangent–tangent correlation using the software FiberApp^[55] (see Experimental Section for further

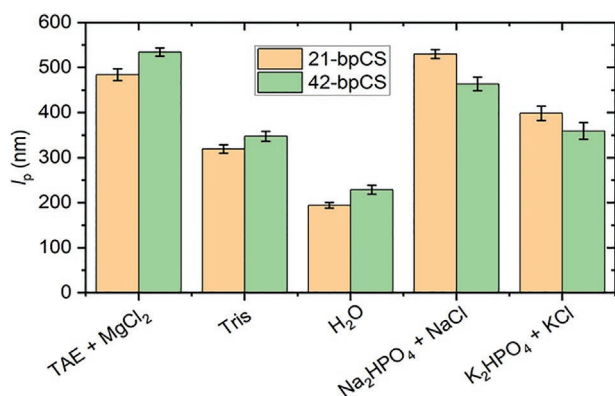


Figure 4. Persistence lengths l_p of the two 6HBs designs in the different Mg^{2+} -free solutions as determined from the AFM images shown in Figures S16–S20, Supporting Information. For each condition, between 79 and 235 individual 6HBs have been evaluated. Error bars represent the errors of the fits (see Figures S21–S25, Supporting Information).

details and Figures S21–S25, Supporting Information for the corresponding fits). The results are shown in **Figure 4**.

In standard TAE/MgCl₂ buffer, both 6HB designs have rather similar persistence lengths of about 490 to 550 nm. This is rather surprising, considering that the MD simulations yield persistence lengths of 6558 and 5322 nm for 21-bpCS and 42-bpCS, respectively (see Figure 2d). At this point, it should be noted that there is some disagreement in the literature regarding the correct determination of persistence lengths from AFM images. There is a large body of works that measured the persistence lengths of semi-flexible biopolymers such as dsDNA,^[56–59] protein filaments,^[60–63] amyloid fibrils,^[64–67] and DNA helix bundles^[68–71] adsorbed at solid surfaces using $s = 2$ as we did in this work. However, it was also argued for dsDNA and dsRNA adsorbed at poly-L-lysine-coated mica surfaces that the immobilized molecules are not equilibrated but kinetically trapped at the surface, resulting in a situation better described by $s = 1$.^[72] It is not clear so far, whether this is also the case for the spermidine-coated mica surfaces used in our experiments. Using $s = 1$ instead of $s = 2$, however, will result in only a doubling of the obtained persistence lengths. While the resulting values between 1000 and 1100 nm would indeed be closer to the experimentally determined persistence lengths of other 6HB designs reported in the literature, which range from 1.9 to 3.3 μm ,^[51,70,73,74] they would still be much smaller than those obtained from the MD simulations in Figure 2. Closer inspection of the corresponding AFM images (Figures S16–S20, Supporting Information) may provide an explanation for this discrepancy. In particular, several of the adsorbed 6HBs exhibit pronounced bends and sharp kinks. This indicates the presence of defects and in particular strand breaks. Such defects may occur during sample handling such as pipetting, spin filtering, and so on, and in general result in a reduced persistence length.^[68,73] On the other hand, the strong electrostatic interactions with the spermidine-modified mica surface during adsorption may also lead to the 6HBs assuming bent and kinked conformations that would not occur in bulk solution.^[52] Even though any visibly damaged or broken 6HBs have been omitted in the analyses, bent and kinked 6HBs were indeed provided that the software could accurately fit their

traces. Therefore, we assume that the experimentally determined persistence lengths are mostly governed by structural defects or non-native conformations, which provides an explanation not only for the lower values compared to the MD simulations but also the observation that the 42-bpCS design has a slightly larger persistence length in TAE/MgCl₂ buffer than 21-bpCS.

Despite this strong influence of defects or non-native conformations, the persistence lengths of both 6HB designs show a remarkable dependence on the environmental conditions. As can be observed in Figure 4, l_p drops to about 300 to 350 nm for both 6HBs when they are transferred into Mg^{2+} -free Tris buffer. In pure H₂O, the decrease is even stronger, resulting in l_p values of only about 200 and 230 nm for 21-bpCS and 42-bpCS, respectively. This continuous decrease in l_p from TAE/MgCl₂ to Tris to H₂O can be explained by the reduction of ionic strength. While TAE/MgCl₂ has millimolar concentrations of Mg^{2+} , Cl⁻, and acetate ions, ionic strength is already greatly reduced in 10 mM Tris and almost negligible in pure H₂O. In the latter case, we expect that electrostatic inter-strand repulsion is compensated solely by residual Mg^{2+} ions bound to the backbone phosphates, whereas in Tris also protonated tris(hydroxymethyl)aminomethane will contribute to the screening of electrostatic repulsion.

In the phosphate-based buffers that feature 200 mM concentrations of NaCl and KCl, respectively, l_p is again closer to its original value for both 6HB designs. This is in line with the well-known fact that monovalent cations are about ten times less efficient in stabilizing DNA duplex structures than Mg^{2+} .^[32,75,76] However, the value of l_p in general is a bit larger in NaCl- than in KCl-containing phosphate buffers. This can be attributed to the fact that K⁺ is again slightly less potent in stabilizing DNA than Na⁺, because it is predominantly binding to the nucleobases and not to the backbone phosphates.^[32,77,78] Furthermore, in both phosphate-based buffers, we find that the 42-bpCS design has a larger persistence length than the 21-bpCS design. To some extent, this may be related to the differences in surface coverage between the two designs that are observed in these buffers (see Figures S19 and S20, Supporting Information). At higher surface coverage, intermolecular interactions may result in the straightening of the adsorbing 6HBs. On the other hand, also the replacement of residual Mg^{2+} ions bound to the backbone phosphates by Na⁺ or K⁺ ions and the accompanying reduction of salt bridges between neighboring double helices may play a role in this context.

While the measured l_p values of both 6HB designs reflect the overall trend of the ionic strength of the solvent, it is rather surprising that a higher ionic strength leads to a larger persistence length. In general, the persistence length of DNA^[79] and other polyelectrolytes^[80] is found to decrease with increasing ionic strength of the solvent because screening of electrostatic interactions results in a behavior closer to that of an uncharged polymer and thus larger flexibility. However, there are also exceptions to this behavior. Collagen proteins, for instance, show a similar dependence as observed in the present experiments, that is, their persistence length may increase with ionic strength.^[81,82] While the origin of this behavior is not completely understood, it was suggested that the presence of certain cosolutes may induce curvature along the collagen backbone.^[82]

For the 6HBs studied in the present work, however, there are additional factors to consider. Most importantly, a lower ionic strength will result in a weaker screening of electrostatic repulsion between neighboring double helices. Stronger inter-helical repulsion will most likely lead to an altered 6HB conformation characterized by a larger diameter and in particular a larger inter-helical spacing.^[83] The latter should then result in a larger persistence length as shown by Schiffels et al.^[51] This, however, is not in line with our observation as the smallest persistence lengths are obtained after transfer into pure H₂O. On the other hand, a lower ionic strength also results in a reduction of the DNA melting temperature. When considering only a single duplex, this effect is rather small and will result in variations of only a few degrees over a wide range of ionic strengths.^[76] The staples of a given DNA origami, however, have a rather broad distribution of melting temperatures^[48] and are subject to mechanical strain resulting from the non-native conformation of the Holliday junctions that comprise the crossovers between neighboring helices.

A decrease in melting temperature at decreased ionic strength in combination with an increased inter-helical repulsion may therefore induce a partial melting of particularly susceptible staple strands. The resulting structural defects will then lead to a smaller persistence length. We thus believe that the combination of both effects, that is, reduced melting temperature and increased electrostatic repulsion between neighboring helices at low ionic strength, is responsible for the observed buffer dependence of the persistence length.

2.4. Resistance against DNase I Digestion

To investigate how the two designs interact with digestion enzymes, the structures were exposed to various concentrations of DNase I (0–200 KU mL⁻¹) and digested for 15 and 150 min. After inactivating the DNase I with sodium dodecyl sulfate (SDS), the samples were analyzed by agarose gel electrophoresis (AGE) (see Experimental Section). The results are shown in Figure 5.

Again, there is a drastic contrast between the two designs. According to the gel analysis, full digestion of the 21-bpCS in

the same time frame as 42-bpCS requires approximately four times higher DNase I concentrations, or alternatively, ten times longer digestion times with the same DNase I concentration. The digestion takes longer for 21-bpCS than 42-bpCS as is evident from the gels (15 and 150 min) in Figure 5. The 21-bpCS digestion progress was also followed by TEM imaging samples in corresponding conditions (Figures S26–S28, Supporting Information).

The differences between the degradation profiles of the two 6HBs are presumably related to the accessibility of the dsDNA to nucleases and the flexibility of the structures, as a similar superstructure-dependent effect has been observed in the enzymatic digestion of DNA origami with different shapes. For example, in the previous work by Ramakrishnan et al.,^[33] flexible DNA origami domains/segments were degraded much more readily by nucleases, essentially serving as initiation sites for the digestion process.

3. Conclusions

To conclude, we studied the effects that crossovers elicit on the mechanical properties and environmental behavior of DNA nanostructures by designing and then experimentally comparing two externally identical DNA origami 6HBs with different crossover spacings of 42 and 21 bp, respectively. The roughly twofold increase in crossover quantity in 21-bpCS resulted in a significant increase in nuclease digestion resistance, but also a decrease in tolerance against low-Mg²⁺ buffers. The increased number of crossovers likely makes the 6HBs less accessible to nucleases, but simultaneously causes the structures to lose malleability. Thus, the 6HBs are more easily denatured when ionic charge screening is reduced in low-Mg²⁺ environments. This type of superstructure-dependent behavior has been hinted at also in previous DNA origami digestion^[33,34] and low-Mg²⁺ studies,^[32,84] and is now systematically confirmed here.

The crossovers of DNA nanostructures have a considerable effect on how they behave in different environmental conditions. When the crossover number is changed, there is interplay between dsDNA accessibility and the malleability of the structures, which allows tuning them either toward increased nuclease resistance or low-Mg²⁺ stability. Low-Mg²⁺ concentrations are frequently required in vitro, for instance to facilitate efficient DNA origami mineralization^[85] or actuation,^[86] and rational crossover engineering may enable the tailoring of a given DNA origami shape toward its anticipated environment. Physiological conditions, however, usually exhibit both low-Mg²⁺ and high nuclease concentrations,^[31] so that crossover engineering may quickly reach its limits. Nevertheless, rational crossover designs may also prove beneficial here, especially when designing DNA origami-based drug carriers.^[11,87] The drug loading capacity of DNA structures depends on the accessibility of dsDNA to drug binding,^[88,89] but simultaneously the stability of the superstructure is also affected: an accessible structure with high loading capacity will presumably be prone to nuclease digestion as well. Rational crossover engineering may thus allow for the synthesis of DNA origami-based drug delivery vehicles with tailored degradation and drug release profiles.^[34]

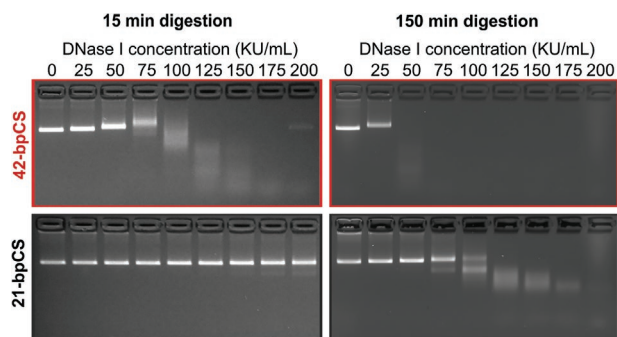


Figure 5. DNase I digestion of 6HBs with different crossover spacings. The 21-bpCS design is digested significantly slower than the 42-bpCS structure. TEM images of the samples corresponding to lanes 3, 4, and 5 in the bottom right gel are shown in Figures S26–S28, Supporting Information.

Finally, optimization of crossover density and arrangement is an independent strategy at the design stage that can be combined with various post-assembly stabilization strategies in order to compensate for specific weaknesses of the former. We thus expect crossover engineering to become a value tool for tailoring DNA origami stability in vitro and in vivo.

4. Experimental Section

DNA Origami Design and Folding: The original 6HB design (42-bpCS) by Bui et al.^[49] was first recreated in caDNAo.^[90] The structure employed the 7249-nt long M13mp18 scaffold, and the scaffold permutation was selected to yield the exact same staple sequences used in the original work by Bui et al. The 21-bpCS variant with its increased number of crossovers was then created by using the same scaffold routing and modifying the staple structure of the 42-bpCS design as described in Section 2. Preliminary validation and structural simulation was performed with CanDo^[5,47] for both designs.

The DNA origami were folded by mixing a 10× molar excess of each staple strand with the scaffold in salt supplemented folding buffer (FOB; ≈200 nm of staples and 20 nm of scaffold in 1× TAE with 10–12.5 mM MgCl₂) and annealing the mixture according to the following thermal ramp: 1) heating the mixture to 90 °C, 2) cooling from 90 to 70 °C at a rate of −1.50 °C min^{−1}, 3) cooling from 70 to 60 °C at a rate of −0.75 °C min^{−1}, and 4) cooling from 60 to 27 °C at a rate of −0.05 °C min^{−1}. After folding, the DNA origami were purified either using spin filtering (see AFM Sample Preparation, Buffers, Imaging, and Analysis) or poly(ethylene glycol) (PEG) precipitation^[91] (see DNase I Digestion). The purified structures were examined with AGE and TEM. Additional figures and further details on folding optimization, folding validation, and structural validation are included in Figures S5–S7, Supporting Information.

Simulation Details: The two structures were simulated using molecular dynamics simulations, and in particular the DNA was modeled using the coarse-grained model oxDNA2.^[92,93] The first step consisted of converting the caDNAo structure into the oxDNA 3D representation using the tacoxDNA package.^[94] The configurations were first relaxed using the reported protocol^[94] and simulated afterward using the LAMMPS implementation,^[95] setting the temperature $T = 300$ K and monovalent salt concentration to 1 M. Electrolytes were accounted implicitly through the Debye–Hückel model for screened electrostatics. The systems were evolved for about 4×10^5 simulation time units, and about 3000 configurations were sampled.

AFM Sample Preparation, Buffers, Imaging, and Analysis: The DNA origami 6HBs were assembled, purified, and the FOB (1× TAE with 10 mM MgCl₂, pH ≈8.5) exchanged by spin filtering using Amicon Ultra filters (Merck) with 100 kDa molecular weight cut-off (MWCO) as previously described.^[32] The buffers used were 1× TAE (40 mM Tris, 20 mM acetic acid, 1 mM EDTA, pH ≈ 8.5), 10 mM Tris (pH ≈8.9), 10 mM Na₂HPO₄ (pH ≈ 8.0), 10 mM Na₂HPO₄ with 200 mM NaCl (pH ≈ 8.5), 10 mM K₂HPO₄ (pH ≈ 8.5), and 10 mM K₂HPO₄ with 200 mM KCl (pH ≈ 8.9). For further details of buffer preparation, see Kieler et al.^[32] Note that no influence on DNA origami stability had been observed for pH 8–9.^[32]

After purification and buffer exchange, the DNA origami concentration was determined using an Implen Nanophotometer P 330 and diluted to 1 nM, after which the sample was immediately immobilized on a mica substrate. For immobilization on non-modified mica (Figure 3), the samples were diluted with 1× TAE buffer supplemented with 10 mM MgCl₂ and incubated on freshly cleaved mica surfaces for 1 min. Then, the mica substrate was rinsed with HPLC-grade water (VWR) and blow-dried in a stream of ultrapure air.

For immobilization on spermidine-modified mica (Figure 4), the samples were diluted in the respective Mg²⁺-free solutions. A 5 mg mL^{−1} spermidine aqueous solution (Alfa Aesar) was dropped onto a freshly

cleaved mica surface and incubated for 5 min. Then, the mica substrate was rinsed with HPLC-grade water to remove excess spermidine. Subsequently, the diluted DNA origami solution was deposited onto the spermidine-coated mica surface. After incubation for 5 min, the mica substrate was rinsed with HPLC-grade water and blow-dried in a stream of ultrapure air.

AFM imaging was performed in air using a Bruker Dimension Icon AFM in ScanAsyst mode with ScanAsyst-Air cantilevers (Bruker) and an Agilent 5500 AFM in intermittent contact mode with HQ:NSC18/Al BS cantilevers (MikroMasch), respectively. Images were recorded with a scan size of $3 \times 3 \mu\text{m}^2$ and a resolution of $1024 \text{ px} \times 1024 \text{ px}$ (see Figures S8–S20, Supporting Information for representative AFM images of all samples).

The persistence lengths of the DNA origami 6HBs immobilized on spermidine-coated mica surfaces were determined using the software FiberApp.^[55] To this end, the recorded AFM images were flattened in Gwyddion^[96] and exported as .tiff files. The .tiff files were opened in FiberApp and the individual 6HBs were manually selected and traced. Care was taken to select only 6HBs that did not have direct contact with neighboring 6HBs in order to avoid any influence of intermolecular interactions. The persistence lengths were then determined for all selected 6HBs in all AFM images recorded for each condition using the tangent–tangent correlation (also called bond correlation) method (see Figures S21–S25, Supporting Information for the plotted values and fits).

DNase I Digestion: For studying the DNase I digestion of DNA origami 6HBs, both types of folded DNA origami structures were first purified of excess staple oligonucleotides using PEG precipitation.^[91] The folded DNA origami structures were diluted to a 5 nM concentration with FOB and mixed in a 1:1 ratio with PEG precipitation buffer (1× TAE, 15% w/v PEG 8000, 505 mM NaCl). The mixture was centrifuged at $14000 \times g$ for 30 min at room temperature (RT), the supernatant was discarded, and the DNA origami pellet was resuspended in the original volume of FOB by incubating the sample overnight at RT.

The DNA origami concentration after purification was determined using a BioTek Eon microplate reader and a Take3 micro-volume plate, and the samples were diluted to 4.5 nM with FOB. 2 μL of DNase I solution (Sigma-Aldrich; 0.2–1.6 KU μL^{−1} in Milli-Q water) was mixed with 16 μL of the 4.5 nM 6HB solution to yield a DNA origami concentration of 4 nM and a DNase I concentration of 25–200 KU mL^{−1} in $0.89 \times$ TAE and 11.1 mM MgCl₂. A control sample with 0 KU mL^{−1} DNase I was prepared by adding 2 μL of Milli-Q water to the sample. After letting the digestion proceed for either 15 or 150 min at RT, the digestion was stopped by inactivating the DNase I by an addition of 2 μL of 1.0% SDS to a final 0.1% SDS concentration.

The digestion outcome was then analyzed with AGE. A 2% agarose gel was prepared in 1× TAE containing 11 mM MgCl₂, and stained with ethidium bromide (0.46 μg mL^{−1} final concentration). To load the digested DNA origami samples on the gel, each 20 μL sample was mixed with 4 μL of 40% sucrose. The gel was run for 45 min at 90 V on an ice bath in a running buffer containing 1× TAE and 11 mM MgCl₂, and imaged after the run under ultraviolet light using a Bio-Rad ChemiDoc MP Imaging System.

Statistical Analysis: For each persistence length value shown in Figure 4, between 79 and 235 individual 6HBs from up to ten AFM images recorded at different positions on the surfaces of two identically treated samples were analyzed using the software FiberApp.^[55] For each buffer condition, the plotted l_p value was obtained from the fit to the $\langle \cos\theta(l) \rangle$ data with the error bar indicating the error of the fit. All $\langle \cos\theta(l) \rangle$ data, fits, fit results, and corresponding R^2 values are shown in Figures S21–S25, Supporting Information.

Supporting Information

Supporting Information is available from the Wiley Online Library or from the author.

Acknowledgements

The authors would like to thank David M. Smith for helpful discussions. Financial support through Emil Aaltonen Foundation, Jane and Aatos Erkko Foundation, Sigrid Jusélius Foundation, Magnus Ehrnrooth Foundation, and Finnish Cultural Foundation (Kalle and Dagmar Välimaa Fund) is gratefully acknowledged. The authors would like to acknowledge the provision of facilities and technical support by Aalto University Bioeconomy Facilities and OtaNano—Nanomicroscopy Center (Aalto-NMC) and Micronova Nanofabrication Center.

Conflict of Interest

The authors declare no conflict of interest.

Data Availability Statement

The data that support the findings of this study are available from the corresponding author upon reasonable request.

Keywords

DNA nanotechnology, endonucleases, persistence length, magnesium, stability

Received: November 29, 2021
Revised: March 14, 2022
Published online: April 1, 2022

- [1] N. C. Seeman, H. F. Sleiman, *Nat. Rev. Mater.* **2018**, *3*, 17068.
- [2] S. Nummelin, J. Kommeri, M. A. Kostiaainen, V. Linko, *Adv. Mater.* **2018**, *30*, 1703721.
- [3] P. W. K. Rothmund, *Nature* **2006**, *440*, 297.
- [4] S. M. Douglas, H. Dietz, T. Liedl, B. Högberg, F. Graf, W. M. Shih, *Nature* **2009**, *459*, 414.
- [5] C. E. Castro, F. Kilchherr, D.-N. Kim, E. L. Shiao, T. Wauer, P. Wortmann, M. Bathe, H. Dietz, *Nat. Methods* **2011**, *8*, 221.
- [6] V. Linko, M. A. Kostiaainen, *Nat. Biotechnol.* **2016**, *34*, 826.
- [7] S. Dey, C. Fan, K. V. Gothelf, J. Li, C. Lin, L. Liu, N. Liu, M. A. D. Nijenhuis, B. Saccà, F. C. Simmel, H. Yan, P. Zhan, *Nat. Rev. Methods Primers* **2021**, *1*, 13.
- [8] S. Surana, A. R. Shenoy, Y. Krishnan, *Nat. Nanotechnol.* **2015**, *10*, 741.
- [9] S. Ramakrishnan, H. Ijäs, V. Linko, A. Keller, *Comput. Struct. Biotechnol. J.* **2018**, *16*, 342.
- [10] H. Bila, E. E. Kurisinkal, M. M. C. Bastings, *Biomater. Sci.* **2019**, *7*, 532.
- [11] A. Keller, V. Linko, *Angew. Chem., Int. Ed.* **2020**, *59*, 15818.
- [12] S. D. Perrault, W. M. Shih, *ACS Nano* **2014**, *8*, 5132.
- [13] H. Auvinen, H. Zhang, A. Kopilow, E. H. Niemelä, S. Nummelin, A. Correia, H. A. Santos, V. Linko, M. A. Kostiaainen, *Adv. Healthcare Mater.* **2017**, *6*, 1700692.
- [14] N. Ponnuswamy, M. M. C. Bastings, B. Nathwani, J. H. Ryu, L. Y. T. Chou, M. Vinther, W. A. Li, F. M. Anastassacos, D. J. Mooney, W. M. Shih, *Nat. Commun.* **2017**, *8*, 15654.
- [15] X. Liu, F. Zhang, X. Jing, M. Pan, P. Liu, W. Li, B. Zhu, J. Li, H. Chen, L. Wang, J. Lin, Y. Liu, D. Zhao, H. Yan, C. Fan, *Nature* **2018**, *559*, 593.
- [16] S. Julin, B. S. Nonappa, V. Linko, M. A. Kostiaainen, *Angew. Chem., Int. Ed.* **2021**, *60*, 827.
- [17] R. Schreiber, S. Kempter, S. Holler, V. Schüller, D. Schiffels, S. S. Simmel, P. C. Nickels, T. Liedl, *Small* **2011**, *7*, 1795.
- [18] W. Sun, E. Boulais, Y. Hakobyan, W. L. Wang, A. Guan, M. Bathe, P. Yin, *Science* **2014**, *346*, 6210.
- [19] J. Shen, W. Sun, D. Liu, T. Schaus, P. Yin, *Nat. Mater.* **2021**, *20*, 683.
- [20] P. Piskunen, B. Shen, A. Keller, J. J. Toppari, M. A. Kostiaainen, V. Linko, *ACS Appl. Nano Mater.* **2021**, *4*, 529.
- [21] A. Heuer-Jungemann, V. Linko, *ACS Cent. Sci.* **2021**, *7*, 1969.
- [22] M. Kalinowski, R. Haug, H. Said, S. Piasecka, M. Kramer, C. Richert, *ChemBioChem* **2016**, *17*, 1150.
- [23] N. Weizenmann, G. Scheidgen-Kleyboldt, J. Ye, C. B. Krause, D. Kauert, S. Helmi, C. Rouillond, R. Seidel, *Nanoscale* **2021**, *13*, 17556.
- [24] S. Ramakrishnan, L. Schärfer, K. Hunold, S. Fricke, G. Grundmeier, M. Schlierf, A. Keller, G. Krainer, *Nanoscale* **2019**, *11*, 16270.
- [25] A. Rajendran, K. Krishnamurthy, A. Giridasappa, E. Nakata, T. Morii, *Nucleic Acids Res.* **2021**, *49*, 7884.
- [26] A. Rajendran, M. Endo, Y. Katsuda, K. Hidaka, H. Sugiyama, *J. Am. Chem. Soc.* **2011**, *133*, 14488.
- [27] T. Gerling, M. Kube, B. Kick, H. Dietz, *Sci. Adv.* **2018**, *4*, eaau1157.
- [28] T. Gerling, H. Dietz, *Angew. Chem., Int. Ed.* **2019**, *58*, 2680.
- [29] F. M. Anastassacos, Z. Zhao, Y. Zeng, W. M. Shih, *J. Am. Chem. Soc.* **2020**, *142*, 3311.
- [30] J. W. Conway, C. K. McLaughlin, K. J. Castor, H. Sleiman, *Chem. Commun.* **2013**, *49*, 1172.
- [31] J. Hahn, S. F. J. Wickham, W. M. Shih, S. D. Perrault, *ACS Nano* **2014**, *8*, 8765.
- [32] C. Kielar, Y. Xin, B. Shen, M. A. Kostiaainen, G. Grundmeier, V. Linko, A. Keller, *Angew. Chem., Int. Ed.* **2018**, *59*, 9470.
- [33] S. Ramakrishnan, B. Shen, M. A. Kostiaainen, G. Grundmeier, A. Keller, V. Linko, *ChemBioChem* **2019**, *20*, 2818.
- [34] H. Ijäs, B. Shen, A. Heuer-Jungemann, A. Keller, M. A. Kostiaainen, T. Liedl, J. A. Ihalainen, V. Linko, *Nucleic Acids Res.* **2021**, *49*, 3048.
- [35] K.-R. Kim, S. J. Kang, A.-Y. Lee, G. Hwang, M. Park, H. Park, S. Kim, K. Hur, H. S. Chung, C. Mao, D.-R. Ahn, *Biomaterials* **2019**, *195*, 1.
- [36] Q. Liu, G. Liu, T. Wang, J. Fu, R. Li, L. Song, Z.-G. Wang, B. Ding, F. Chen, *ChemPhysChem* **2017**, *18*, 2977.
- [37] A. Stopar, L. Coral, S. Di Giacomo, A. F. Adedeji, M. Castronovo, *Nucleic Acids Res.* **2018**, *46*, 995.
- [38] A. R. Chandrasekaran, J. Vilcapoma, P. Dey, S. W. Wong-Deyrup, B. K. Dey, K. Halvorsen, *J. Am. Chem. Soc.* **2020**, *142*, 6814.
- [39] A. Suma, A. Stopar, A. W. Nicholson, M. Castronovo, V. Carnevale, *Nucleic Acids Res.* **2020**, *48*, 4672.
- [40] H. Dietz, S. M. Douglas, W. M. Shih, *Science* **2009**, *325*, 725.
- [41] C. Plesa, A. N. Ananth, V. Linko, C. Gülcher, A. J. Katan, H. Dietz, C. Dekker, *ACS Nano* **2014**, *8*, 35.
- [42] C. E. Castro, H. J. Su, A. E. Marras, L. Zhou, J. Johnson, *Nanoscale* **2015**, *7*, 5913.
- [43] K. E. Dunn, F. Dannenberg, T. E. Ouldrige, M. Kwiatkowska, A. J. Turberfield, J. Bath, *Nature* **2015**, *525*, 82.
- [44] Z. Ma, K. Kawai, Y. Hirai, T. Tsuchiya, O. Tabata, *Jpn. J. Appl. Phys.* **2017**, *56*, 06GJ02.
- [45] N. Stephanopoulos, *ChemBioChem* **2019**, *20*, 2191.
- [46] A. R. Chandrasekaran, *Nat. Rev. Chem.* **2021**, *5*, 225.
- [47] D.-N. Kim, F. Kilchherr, H. Dietz, M. Bathe, *Nucleic Acids Res.* **2012**, *40*, 2862.
- [48] S. Ramakrishnan, G. Krainer, G. Grundmeier, M. Schlierf, A. Keller, *Nanoscale* **2016**, *8*, 10398.
- [49] H. Bui, C. Onodera, C. Kidwell, Y. Tan, E. Graugnard, W. Kuang, J. Lee, W. B. Knowlton, B. Yurke, W. L. Hughes, *Nano Lett.* **2010**, *10*, 3367.
- [50] G. Lamour, J. B. Kirkegaard, H. Li, T. P. J. Knowles, J. Gsponer, *Source Code Biol. Med.* **2014**, *9*, 16.
- [51] D. Schiffels, T. Liedl, D. K. Fygenon, *ACS Nano* **2013**, *7*, 6700.

- [52] Y. Xin, A. A. Zargariantabrizi, G. Grundmeier, A. Keller, *Molecules* **2021**, *26*, 4798.
- [53] A. Wahab, S. Mahiuddin, G. Hefter, W. Kunz, B. Minofar, P. Jungwirth, *J. Phys. Chem. B* **2005**, *109*, 24108.
- [54] B. Minofar, R. Vácha, A. Wahab, S. Mahiuddin, W. Kunz, P. Jungwirth, *J. Phys. Chem. B* **2006**, *110*, 15939.
- [55] I. Usov, R. Mezzenga, *Macromolecules* **2015**, *48*, 1269.
- [56] S. Mantelli, P. Muller, S. Harlepp, M. Maaloum, *Soft Matter* **2011**, *7*, 3412.
- [57] J. Moukhtar, C. Faivre-Moskalenko, P. Milani, B. Audit, C. Vaillant, E. Fontaine, F. Mongelard, G. Lavorel, P. St-Jean, P. Bouvet, F. Argoul, A. Arneodo, *J. Phys. Chem. B* **2010**, *114*, 5125.
- [58] D. Murugesapillai, S. Bouaziz, L. J. Maher, N. E. Israeloff, C. E. Cameron, M. C. Williams, *Nanoscale* **2017**, *9*, 11327.
- [59] B. Kundukad, P. Cong, J. R. C. van der Maarel, P. S. Doyle, *Nucleic Acids Res.* **2013**, *41*, 8280.
- [60] A. Ott, M. Magnasco, A. Simon, A. Libchaber, *Phys. Rev. E* **1993**, *48*, R1642.
- [61] N. Mücke, L. Kreplak, R. Kirmse, T. Wedig, H. Herrmann, U. Aebi, J. Langowski, *J. Mol. Biol.* **2004**, *335*, 1241.
- [62] N. Mücke, K. Klenin, R. Kirmse, M. Bussiek, H. Herrmann, M. Hafner, J. Langowski, *PLoS One* **2009**, *4*, e7756.
- [63] H. Takatsuki, E. Bengtsson, A. Månsson, *Biochim. Biophys. Acta Gen. Subj.* **2014**, *1840*, 1933.
- [64] J. Adamcik, J.-M. Jung, J. Flakowski, P. De Los Rios, G. Dietler, R. Mezzenga, *Nat. Nanotechnol.* **2010**, *5*, 423.
- [65] I. Usov, J. Adamcik, R. Mezzenga, *ACS Nano* **2013**, *7*, 10465.
- [66] C. C. vandenAkker, M. F. M. Engel, K. P. Velikov, M. Bonn, G. H. Koenderink, *J. Am. Chem. Soc.* **2011**, *133*, 18030.
- [67] A. Makky, L. Bousset, K. Madiona, R. Melki, *Biophys. J.* **2020**, *119*, 2497.
- [68] C. Lee, K. S. Kim, Y.-J. Kim, J. Y. Lee, D.-N. Kim, *ACS Nano* **2019**, *13*, 8329.
- [69] Y.-J. Kim, J. Lim, D.-N. Kim, *Small* **2022**, *18*, 2103779.
- [70] C. Schuldt, J. Schnauß, T. Händler, M. Glaser, J. Lorenz, T. Golde, J. A. Käs, D. M. Smith, *Phys. Rev. Lett.* **2016**, *117*, 197801.
- [71] C. Lee, Y.-J. Kim, K. S. Kim, J. Y. Lee, D.-N. Kim, *Nucleic Acids Res.* **2021**, *49*, 12591.
- [72] J. A. Abels, F. Moreno-Herrero, T. van der Heijden, C. Dekker, N. H. Dekker, *Biophys. J.* **2005**, *88*, 2737.
- [73] T. Liedl, B. Högberg, J. Tytell, D. E. Ingber, W. M. Shih, *Nat. Nanotechnol.* **2010**, *5*, 520.
- [74] D. J. Kauert, T. Kurth, T. Liedl, R. Seidel, *Nano Lett.* **2011**, *11*, 5558.
- [75] S.-I. Nakano, M. Fujimoto, H. Hara, N. Sugimoto, *Nucleic Acids Res.* **1999**, *27*, 2957.
- [76] S. Ramakrishnan, G. Krainer, G. Grundmeier, M. Schlierf, A. Keller, *Small* **2017**, *13*, 1702100.
- [77] Y. Cheng, N. Korolev, L. Nordenskiöld, *Nucleic Acids Res.* **2006**, *34*, 686.
- [78] Y. Xin, S. Martinez Rivadeneira, G. Grundmeier, M. Castro, A. Keller, *Nano Res.* **2020**, *13*, 3142.
- [79] G. S. Manning, *Biophys. J.* **2006**, *91*, 3607.
- [80] H. K. Murnen, A. M. Rosales, A. V. Dobrynin, R. N. Zuckermann, R. A. Segalman, *Soft Matter* **2013**, *9*, 90.
- [81] H. H. Lovelady, S. Shashidhara, W. G. Matthews, *Biopolymers* **2013**, *101*, 329.
- [82] N. Rezaei, A. Lyons, N. R. Forde, *Biophys. J.* **2018**, *115*, 1457.
- [83] S. Fischer, C. Hartl, K. Frank, J. O. Rädler, T. Liedl, B. Nickel, *Nano Lett.* **2016**, *16*, 4282.
- [84] V. Linko, B. Shen, K. Tapio, J. J. Toppari, M. A. Kostianen, S. Tuukkanen, *Sci. Rep.* **2015**, *5*, 15634.
- [85] L. Nguyen, M. Döblinger, T. Liedl, A. Heuer-Jungemann, *Angew. Chem., Int. Ed.* **2019**, *58*, 912.
- [86] F. Kroener, L. Traxler, A. Heerwig, U. Rant, M. Mertig, *ACS Appl. Mater. Interfaces* **2019**, *11*, 2295.
- [87] E. L. Coleridge, K. E. Dunn, *Biomed. Phys. Eng. Express* **2020**, *6*, 065030.
- [88] F. Kollmann, S. Ramakrishnan, B. Shen, G. Grundmeier, M. A. Kostianen, V. Linko, A. Keller, *ACS Omega* **2018**, *3*, 9441.
- [89] H. L. Miller, S. Contera, A. J. M. Wollman, A. Hirst, K. E. Dunn, S. Schröter, D. O'Connell, M. C. Leake, *Nanotechnology* **2020**, *31*, 235605.
- [90] S. M. Douglas, A. H. Marblestone, S. Teerapittayanon, A. Vazquez, G. M. Church, W. M. Shih, *Nucleic Acids Res.* **2009**, *37*, 5001.
- [91] E. Stahl, T. G. Martin, F. Praetorius, H. Dietz, *Angew. Chem., Int. Ed.* **2014**, *53*, 12735.
- [92] T. E. Ouldrige, A. A. Louis, J. P. K. Doye, *J. Chem. Phys.* **2011**, *134*, 085101.
- [93] B. E. K. Snodin, F. Randisi, M. Mosayebi, P. Šulc, J. S. Schreck, F. Romano, T. E. Ouldrige, R. Tsukanov, E. Nir, A. A. Louis, J. P. K. Doye, *J. Chem. Phys.* **2015**, *142*, 234901.
- [94] A. Suma, E. Poppleton, M. Matthies, P. Šulc, F. Romano, A. A. Louis, J. P. K. Doye, C. Micheletti, L. Rovigatti, *J. Comput. Chem.* **2019**, *40*, 2586.
- [95] O. Henrich, Y. A. G. Fosado, T. Curk, T. E. Ouldrige, *Eur. Phys. J. E* **2018**, *41*, 57.
- [96] D. Nečas, P. Klapetek, *Open Phys.* **2012**, *10*, 181.